Supplement of The Cryosphere, 18, 3513–3531, 2024
https://doi.org/10.5194/tc-18-3513-2024-supplement

The Cryosphere
Open Access

Supplement of

Spatial variation in the specific surface area of surface snow measured along the traverse route from the coast to Dome Fuji, Antarctica, during austral summer

Ryo Inoue et al.

Correspondence to: Ryo Inoue (inoue.ryo@nipr.ac.jp)

Note S1: Calibration of the reflected light intensity into reflectance

A handheld integrating sphere snow grain sizer (HISSGraS) measures the near-infrared (NIR) reflectance of snow using an integrating sphere. The InGaAs photodiode, attached inside the integrating sphere, collects the light reflected by a snow sample and outputs a light intensity signal. The signal is then converted to reflectance (R) using a calibration curve derived from measurements on six reflectance standards (5–99%). However, the calibration curve is sensitive to the instrument temperature due to the temperature sensitivity of the laser-diode emission. We describe the method for calibrating the temperature-dependent output signal into R, applicable to the temperature range for our study (−35 to 5°C), following Aoki et al. (2023).

For the temperature correction of the output signal, HISSGraS simultaneously records the temperature near the laser diode along with the output signal of light intensity. We first established the relationship between the laser-diode temperature and the HISSGraS output signal for the six reflectance standards (5–99%). Figure S1a shows 112 output signals for each standard, measured at temperatures between −35 and 5°C during our observation campaign in Antarctica from 12 November 2021 to 31 January 2022. These data show a temperature sensitivity of approximately −1% K^{-1} and can be fitted by cubic curves. Then, we obtain output signals at arbitrary temperatures using the cubic curves. Figure S1b shows output signals at 0, −10, −20, and −30°C as examples, plotted against the reflectance of standards. Obtaining a fitting curve to the output signals using quadratic functions (solid line in Fig. S1b), we can calibrate the output signal into R at arbitrary temperatures. Here, the coefficients of the quadratic functions are parameterized as cubic functions of temperature with relative standard errors of 0.1%, providing the following calibration formula:

$$R = aX^2 + bX + c, \quad \text{(S1)}$$

$$a = -7.2 \times 10^{-12}\, T^3 - 6.7 \times 10^{-10}\, T^2 - 3.41 \times 10^{-8}\, T - 1.753 \times 10^{-6}, \quad \text{(S2)}$$

$$b = 3.8 \times 10^{-8}\, T^3 + 4.3 \times 10^{-6}\, T^2 + 2.95 \times 10^{-4}\, T + 3.091 \times 10^{-2}, \quad \text{(S3)}$$

$$c = -9.5 \times 10^{-5}\, T^3 - 4.0 \times 10^{-3}\, T^2 - 5 \times 10^{-3}\, T - 10.97. \quad \text{(S4)}$$

Here, X represents the output signal (count), a, b, and c are regression coefficients, and T represents laser-diode temperature (°C). The R derived from this formula overlaps the fitting curves in Fig. S1b.

The temperature correction reduces errors in SSA measurements, which are caused by temperature changes during an observation activity due to the laser-diode heating by repeated light emissions or the insufficient adjustment of instrument temperature to ambient temperature. Moreover, the temperature correction eliminates the need for adjusting the laser-diode temperature to ambient temperature before measurement, which typically requires 30 minutes (Aoki et al., 2023), and measuring six reflectance standards necessarily before (or after) all measurement activities.

Note S2: Potential error in broadband albedo derived from HISSGraS measurement

To evaluate the potential error in broadband albedo derived from the surface snow grain size measured with HISSGraS, we compared the albedo values calculated for a snow layer with homogeneous snow grain size to those calculated when the snow grain size of the subsurface layer differs from the surface layer. Broadband albedos were calculated using a physically based snow albedo model (Aoki et al., 2011), which assumes two snow layers. The snow grain shape employed was a spherical particle model, with radii (SSA) in the two snow layers set at 50 μm (65.4 $m^2\ kg^{-1}$), 200 μm (16.4 $m^2\ kg^{-1}$), and 1000 μm (3.3 $m^2\ kg^{-1}$), representing average snow grain radii for new snow, fine-grained old snow, and old snow near the melting point, respectively (Wiscombe and Warren, 1980). The thickness of the top layer was assumed to be the critical snow depth (CSD) for monochromatic albedo at 1310 nm, the laser wavelength of the HISSGraS. The CSD is defined as the depth at which the monochromatic albedo at this wavelength closely approximates (assumed to be 99% in this study) the albedo of a semi-infinitely thick snow layer and no longer depends on the snow grain size in deeper layers. For a snow density of 200 kg m^{-3}, the CSD values are 8.3 mm, 21.1 mm, and 37.1 mm for snow grain radii (r_s) of 50, 200, and 1000 μm, respectively. The thickness of the bottom layer in the two-layer snow model was assumed to be semi-infinite. Snow contamination is held constant at a concentration of 1.0 ng L^{-1} black carbon across all snow layers, based on in-situ measurements along the route from S16 to Mizuho (Kinase et al., 2020). The atmospheric conditions include assumptions of both clear sky and cloudy sky. Considering that the solar zenith angle (θ_0) at local solar noon on the summer solstice is 44.5° and 54.0° at S16 and Dome Fuji, respectively, we calculated the broadband albedos for $\theta_0 > 45°$.

Figure S2 presents the simulated broadband albedo under clear sky (Fig. S2a) and cloudy sky (Fig. S2b) conditions for various combinations of three types of r_s across the two snow layers. When the r_s values in the two snow layers are the same and correspond to the HISSGraS measurement, the simulated broadband albedo corresponds with that expected from the HISSGraS measurement. When the r_s values differ between the top and bottom layers, the potential variability in broadband albedos for each r_s in the top layer is calculated. The difference in albedo between cases where the snow grain size is the same and differs between the two snow layers represents a potential error in the broadband albedo estimated from the surface snow grain size measured with the HISSGraS. The maximum estimated error is 0.05 when the r_s of the top and bottom layers are 1000 μm and 50 μm, respectively, at $\theta_0 = 45°$ under clear sky conditions. This error remains consistent across all θ_0 under cloudy conditions. In this study, the surface snow SSA measured with HISSGraS in Antarctica predominantly falls within the range of 50 μm to 200 μm (Fig. 7). For this range, the estimated maximum error is 0.03 when the r_s for the top and bottom layers are 50 μm and 1000 μm, respectively, under the same θ_0 conditions.

Table S1: In situ observation sites for snow SSA (or r_{eff}) in the top few meters of firn in Antarctica.

Area	Latitude (°)	Longitude (°)[a]	Number of observation spots	Sample / Depth	Instrument	Reference
Dronning Maud Land	−76 to −71	−7 to 20	3 spots	Core / 10–12 m	X-ray CT	Linow et al. (2012)
Kohnen Station	75.0	0.1	46 m transect	Near-surface firn / 1.1 m	Snow Micro Pen	Proksch et al. (2015)
Kohnen Station	75.0	0.1	(1) 1 spot (2) Multi spots along a 100 m transect	(1) Surface snow (2) Surface snow	(1) Albedometer (2) IceCube	Carlsen et al. (2017)
Dome Fuji	−78 to −77	39–41	4 spots	Core / 10 m	Line scanner of NIR reflectance	Inoue et al. (2024)
S16 – Dome Fuji	−78 to −69	39–45	2139 spots along a 1051 km traverse route[b]	Surface snow	HISSGraS	This study
Inland plateau of Wilkes Land	−80 to −75	106–126	7 spots	Core or borehole / 4–18 m	ASSSAP[c] or POSSSUM[d]	Picard et al. (2022)
Dome C	−75.1	123.3	1 spot	Pit wall / 3 m	NIR photography	Brucker et al. (2011)
Dome C	−75.1	123.3	2 spots	Borehole / 8 m	POSSSUM	Picard et al. (2014)
Dome C	−75.1	123.3	1 spot	Surface hoar	Ice Cube	Gallet et al. (2014)
Dome C	−75.1	123.3	(1) 1 spot (2) 632 spots within an area of ~ 1000 m^2 (3) 130 spots with > 5 m intervals	(1) Surface snow (2) Surface snow (3) Pit wall / 0.5 m	(1) Albedometer (2) ASSSAP (3) ASSSAP	Libois et al. (2014; 2015)
Dome C	−75.1	123.3	10 spots	Core / 11–80 m	POSSSUM	Leduc-Leballeur et al. (2015)
Dome C	−75.1	123.3	1 spot	Surface snow	Albedometer	Picard et al. (2016)
Point Barnola	−75.7	123.3	1 spot	Pit sample / 3 m	X-ray CT	Calonne et al. (2017)
Dumont D'Urville – Dome C	−76 to −68	123–139	(1) 8 spots along a ~ 1200 km traverse route (2) 13 spots at Dome C	Pit sample / 0.7 m	Ice Cube	Gallet et al. (2011)
Adélie Land	−70 to −67	134–142	11 spots	Core / 3–9 m	ASSSAP	Picard et al. (2022)
Adélie Coast	−66.7	139.8	2 spots	Surface snow	Albedometer	Arioli et al. (2023)
Hercules Dome	−86	−105	1 spot	Core / 15 m	X-ray CT	Hörhold et al. (2009); Linow et al. (2012)
Aboa Station	−73.1	−13.4	8 spots	Surface snow	Radiometer	Pirazzini et al. (2015)

[a] Listed in the ascending order of longitude. [b] Measurements were missed at 11 surfaces out of 215 sets of 10 different surface measurements. [c] Snow Specific Surface Area Profiler (Libois et al., 2015). [d] Profiler Of Snow Specific Surface area Using shortwave infrared reflectance Measurement (Arnaud et al., 2011).

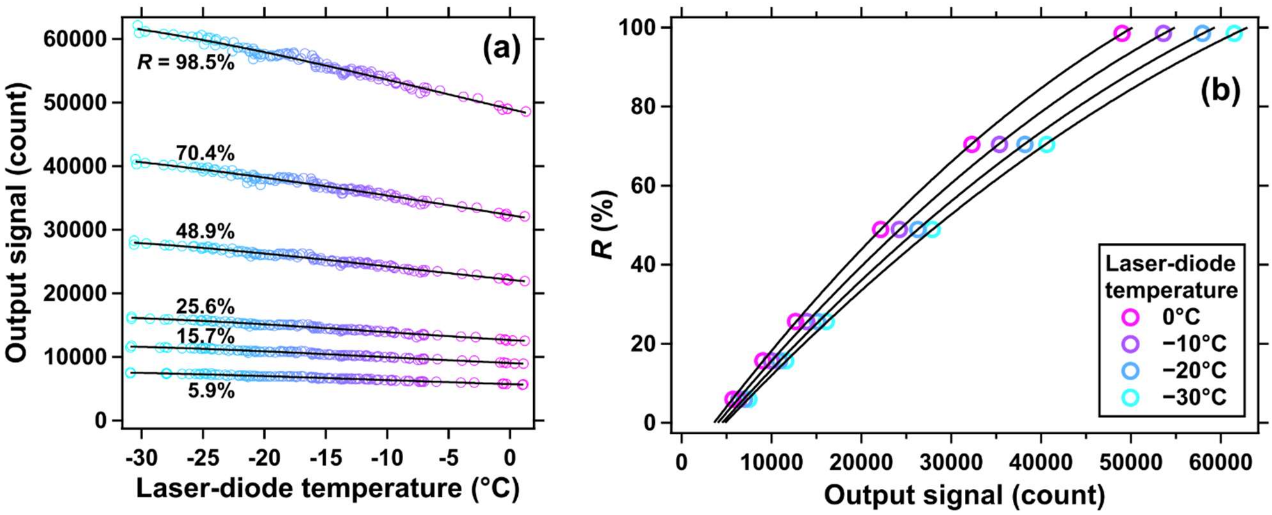

Figure S1: Calibration of the HISSGraS output signal (reflected light intensity) into reflectance *R*. (a) Relationship between laser-diode temperature and the HISSGraS output signal for six reflectance standards (5–99%). The output signals were measured during our observation campaign in Antarctica from 12 November 2021 to 31 January 2022. Marker colors indicate laser-diode temperature. Data are fitted using cubic functions (black lines). (b) Output signals calculated from the cubic curves in (a) at 0, −10, −20, and −30°C, plotted against the reflectance of standards. Data are fitted using quadratic functions (black lines).

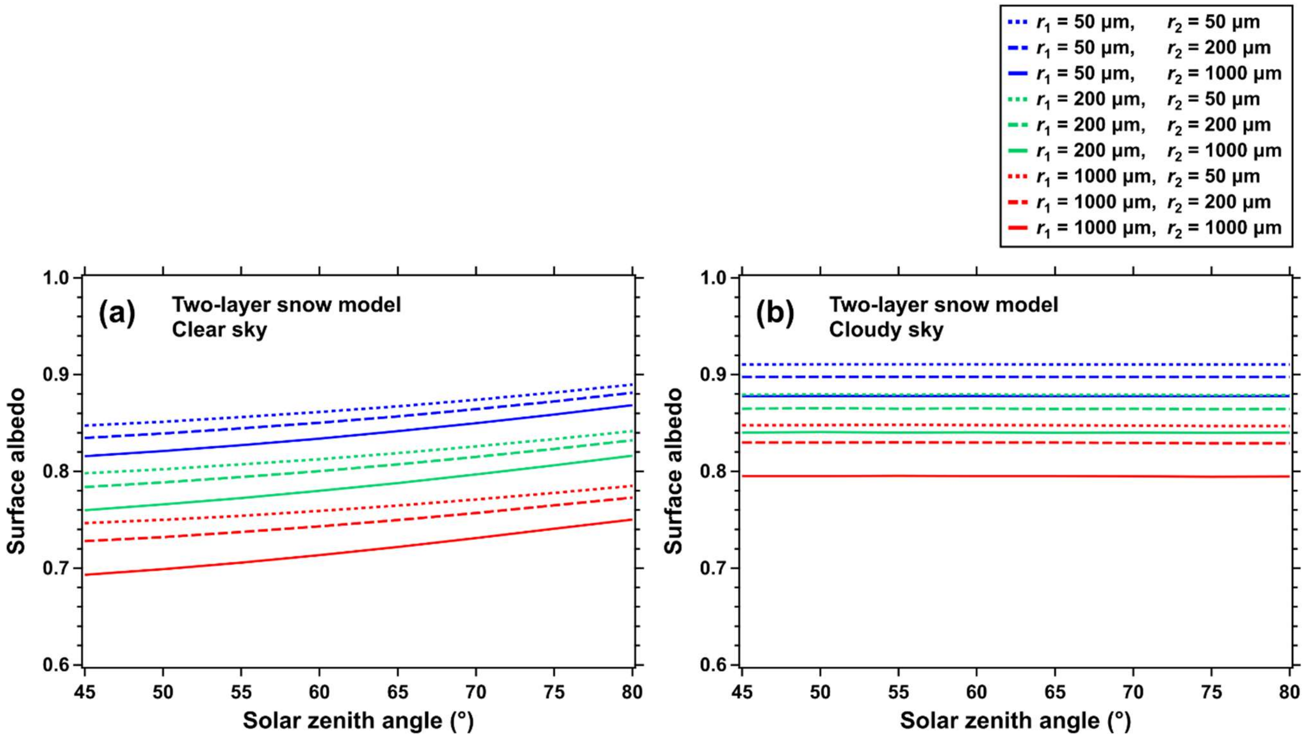

Figure S2: Theoretically calculated broadband albedos under (a) clear sky and (b) cloudy sky for the combination of r_s = 50, 200, and 1000 μm in the two-layer snow model as a function of θ_0 simulated with a physically based snow albedo model.

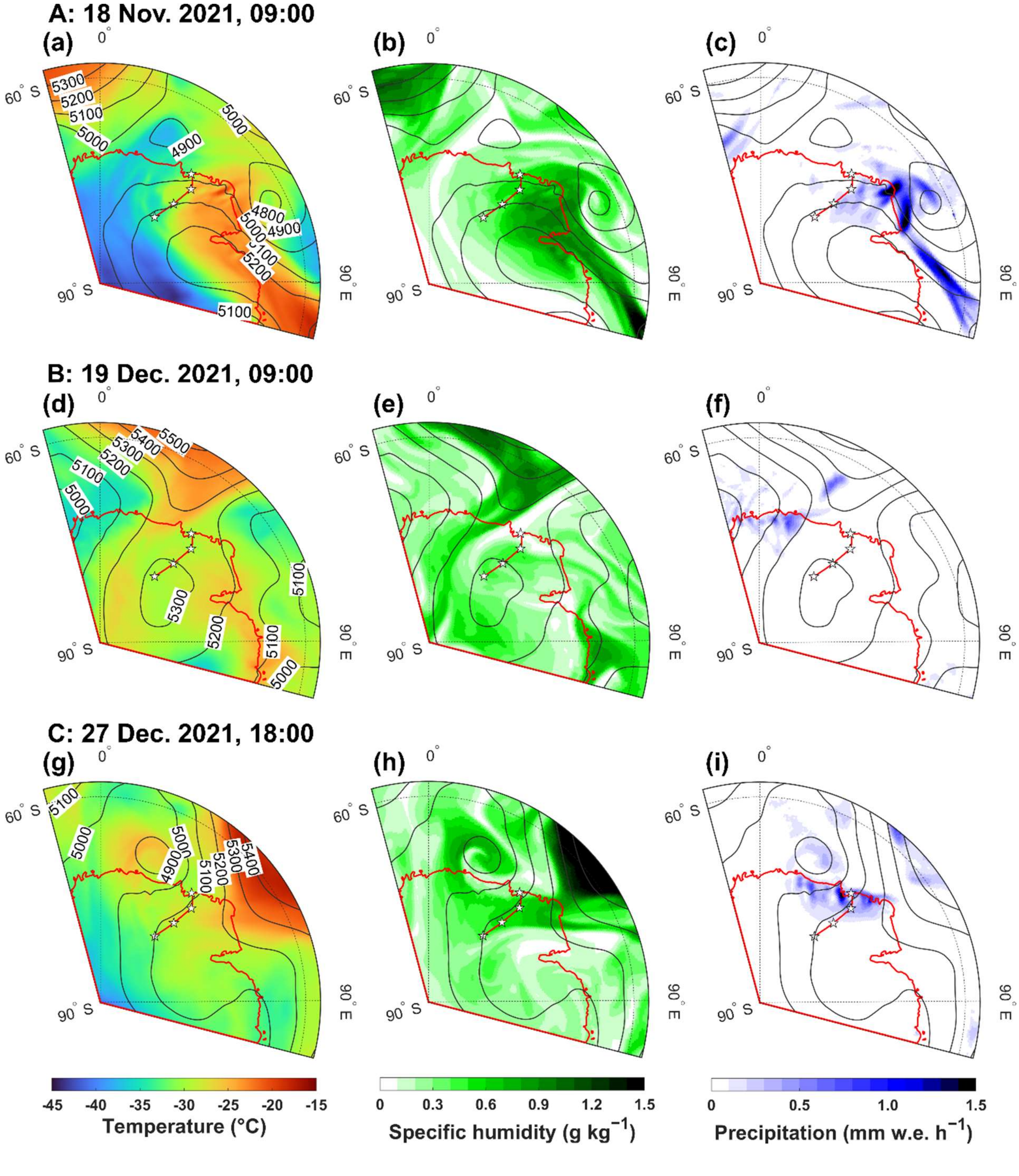
A: 18 Nov. 2021, 09:00
B: 19 Dec. 2021, 09:00
C: 27 Dec. 2021, 18:00
(a)
(b)
(c)
(d)
(e)
(f)
(g)
(h)
(i)
0°
60° S
90° S
90° E
Temperature (°C)
Specific humidity (g kg^{-1})
Precipitation (mm w.e. h^{-1})

Figure S3: Meteorological fields during the events A, B, and C indicated in Figs. 3 and 4 in the main text, derived from the ERA5 reanalysis, the 5th generation global climate reanalysis conducted by the European Centre for Medium-Range Weather Forecasts (Hersbach et al., 2020). The red line in each panel indicates the Antarctic coastline and the traverse route between S16 and Dome Fuji. Stars indicate major sites along the traverse route mentioned in the main text. Contours indicate the 500 hPa geopotential height (m). (a) Temperature at 500 hPa geopotential height, (b) specific humidity at 500 hPa geopotential height, and (c) precipitation at 9:00 LT on 18 November 2021, when we experienced a severe blizzard at Mizuho (second star from the coast). A blocking ridge intrudes from Princess Elizabeth Land toward Dome Fuji, transporting warm, moist air and precipitation to the traverse route along the western side of the blocking ridge. The space between the isoline of the 500 hPa geopotential height is narrow on Mizuho, and the total precipitation during the blizzard event from 17 to 19 November is 10 mm w.e. at Mizuho. (d, e, f) The same as (a, b, c) but for 9:00 LT on 19 December 2021, after which melt-freeze crusts with a low SSA (~ 7 m^2 kg^{-1}) were observed at the surface of S16 (first star from the coast). S16 is located under high atmospheric pressure with low specific humidity and no precipitation. (g, h, i) The same as (a, b, c) but for 18:00 LT on 27 December 2021, when heavy snowfall was observed in the middle area of the traverse route. Air masses with high specific humidities are advected from low latitudes along the east side of a cyclone on the coast of east Dronning Maud Land (DML), and the space between the isolines of the 500 hPa geopotential height expands toward the interior around the traverse route.

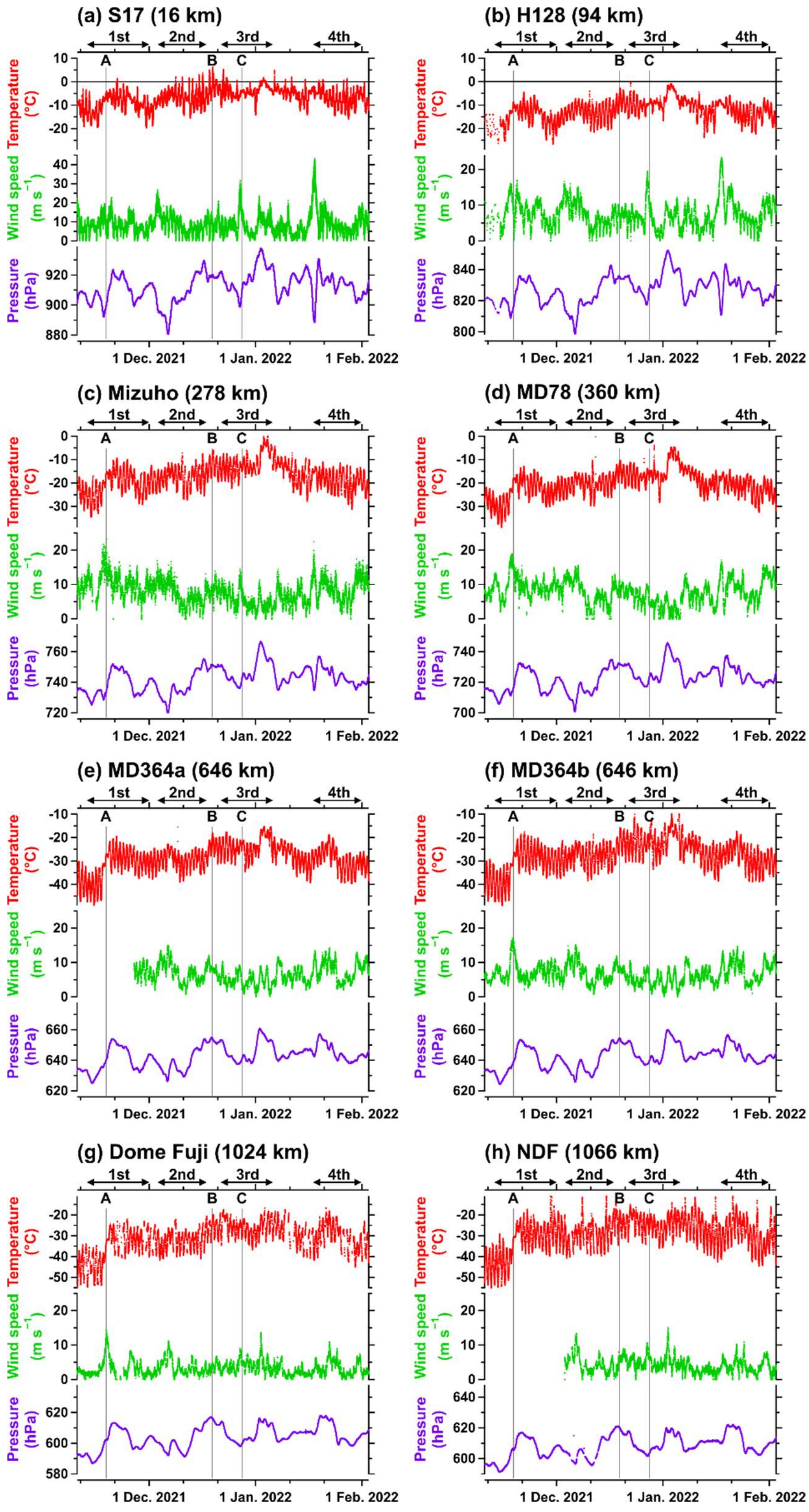

Figure S4: Air temperature, wind speed, and air pressure between 12 November 2021 and 31 January 2022, recorded at (a) S17, (b) H128, (c) Mizuho, (d) MD78, (e) MD364a, (f) MD364b, (g) Dome Fuji, and (h) NDF AWSs. Distances from the coast are shown in parentheses after the AWS names. The double-headed arrows above each panel represent periods for the four traverses. The vertical lines and capital alphabets A, B, and C in each panel indicate meteorological events whose ERA5 meteorological fields in DML are presented in Fig. S3.

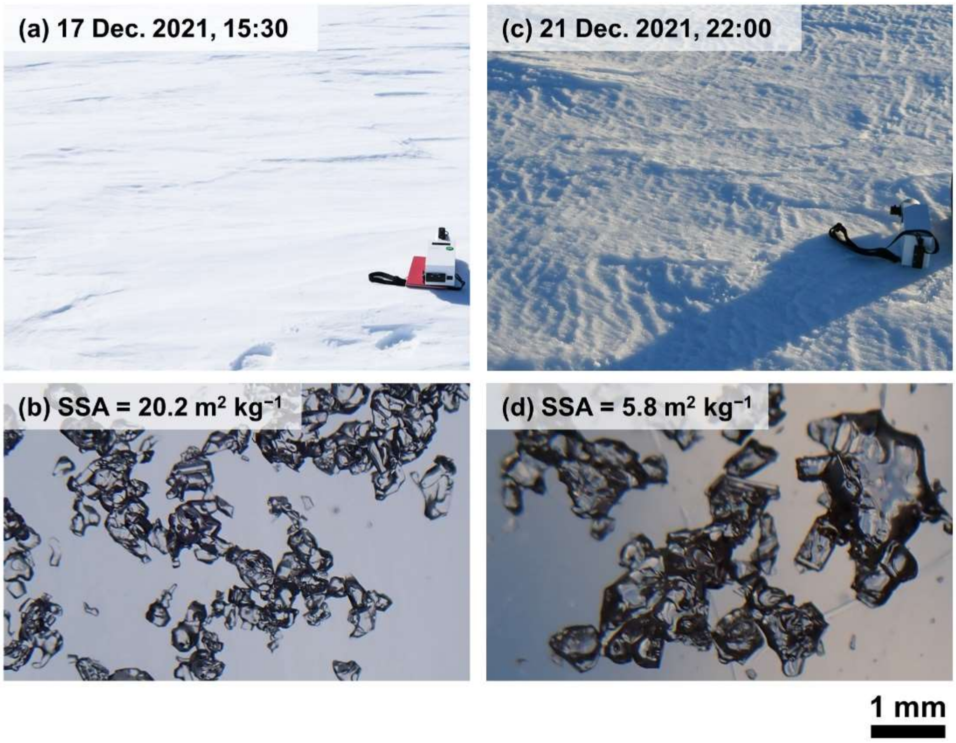

Figure S5: Photographs of the surface at S16 with HISSGraS (0.3 × 0.1 × 0.1 m^3 volume) on the surface and snow crystals (a, b) before event B (indicated in Figs. 3 and 4 in the main text) at 15:30 LT on 17 December 2021 and (c, d) after event B at 22:00 LT on 21 December 2021. The surface becomes rough, with melt-freeze crusts appearing between the period.

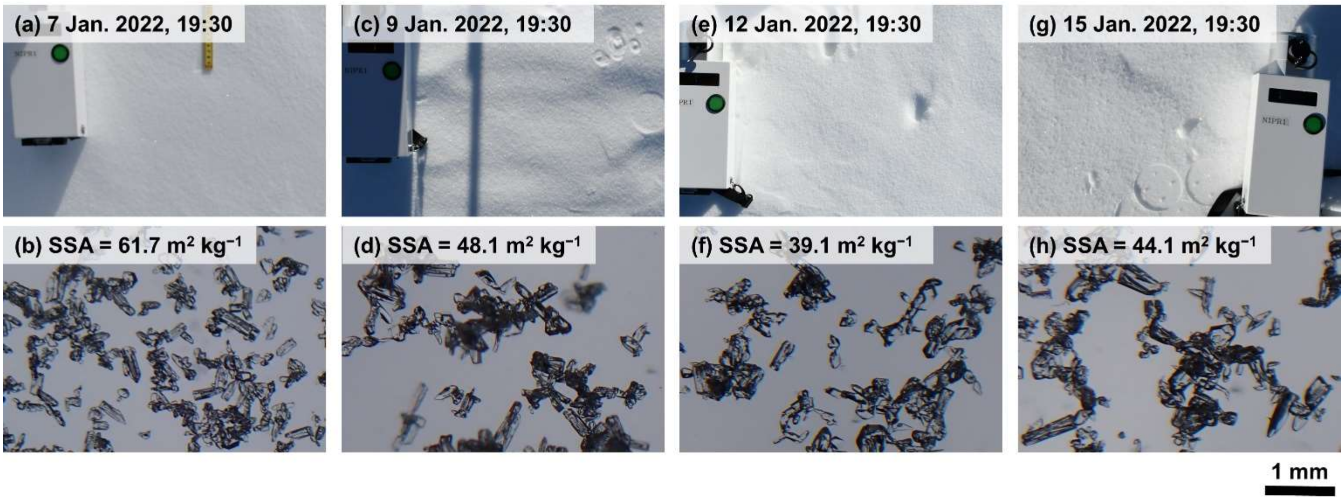

Figure S6: Photographs of the surface at Dome Fuji with HISSGraS on the surface and snow crystals. (a, b) 19:30 LT on 7 January, (c, d) 19:30 LT on 9 January, (e, f) 19:30 LT on 12 January, and (g, h) 19:30 LT on 15 January 2022. Circular marks on the surface are traces made by pressing the glass window in front of HISSGraS.

References

Aoki, T., Kuchiki, K., Niwano, M., Kodama, Y., Hosaka, M., and Tanaka, T.: Physically based snow albedo model for calculating broadband albedos and the solar heating profile in snowpack for general circulation models, J. Geophys. Res. Atmos., 116, D11114, https://doi.org/10.1029/2010JD015507, 2011.

Aoki, T., Hachikubo, A., Nishimura, M., Hori, M., Niwano, M., Tanikawa, T., Sugiura, K., Inoue, R., Yamaguchi, S., Matoba, S., Shimada, R., Ishimoto, H., and Gallet, J.-C.: Development of a handheld integrating sphere snow grain sizer (HISSGraS), Ann. Glaciol., 1–12, https://doi.org/10.1017/aog.2023.72, 2023.

Arioli, S., Picard, G., Arnaud, L., and Favier, V.: Dynamics of the snow grain size in a windy coastal area of Antarctica from continuous in situ spectral-albedo measurements, The Cryosphere, 17, 2323–2342, https://doi.org/10.5194/tc-17-2323-2023, 2023.

Arnaud, L., Picard, G., Champollion, N., Domine, F., Gallet, J. C., Lefebvre, E., Fily, M., and Barnola, J. M.: Measurement of vertical profiles of snow specific surface area with a 1 cm resolution using infrared reflectance: instrument description and validation, J. Glaciol., 57, 17–29, https://doi.org/10.3189/002214311795306664, 2011.

Brucker, L., Picard, G., Arnaud, L., Barnola, J.-M., Schneebeli, M., Brunjail, H., Lefebvre, E., and Fily, M.: Modeling time series of microwave brightness temperature at Dome C, Antarctica, using vertically resolved snow temperature and microstructure measurements, J. Glaciol., 57, 171–182, https://doi.org/10.3189/002214311795306736, 2011.

Calonne, N., Montagnat, M., Matzl, M., and Schneebeli, M.: The layered evolution of fabric and microstructure of snow at Point Barnola, Central East Antarctica, Earth Planet. Sci. Lett., 460, 293–301, https://doi.org/10.1016/j.epsl.2016.11.041, 2017.

Carlsen, T., Birnbaum, G., Ehrlich, A., Freitag, J., Heygster, G., Istomina, L., Kipfstuhl, S., Orsi, A., Schäfer, M., and Wendisch, M.: Comparison of different methods to retrieve optical-equivalent snow grain size in central Antarctica, The Cryosphere, 11, 2727–2741, https://doi.org/10.5194/tc-11-2727-2017, 2017.

Gallet, J.-C., Domine, F., Arnaud, L., Picard, G., and Savarino, J.: Vertical profile of the specific surface area and density of the snow at Dome C and on a transect to Dumont D'Urville, Antarctica – albedo calculations and comparison to remote sensing products, The Cryosphere, 5, 631–649, https://doi.org/10.5194/tc-5-631-2011, 2011.

Gallet, J.-C., Domine, F., Savarino, J., Dumont, M., and Brun, E.: The growth of sublimation crystals and surface hoar on the Antarctic plateau, The Cryosphere, 8, 1205–1215, https://doi.org/10.5194/tc-8-1205-2014, 2014.

Hersbach, H., Bell, B., Berrisford, P., Hirahara, S., Horányi, A., Muñoz-Sabater, J., Nicolas, J., Peubey, C., Radu, R., Schepers, D., Simmons, A., Soci, C., Abdalla, S., Abellan, X., Balsamo, G., Bechtold, P., Biavati, G., Bidlot, J., Bonavita, M., De Chiara, G., Dahlgren, P., Dee, D., Diamantakis, M., Dragani, R., Flemming, J., Forbes, R., Fuentes, M., Geer, A., Haimberger, L., Healy, S., Hogan, R. J., Hólm, E., Janisková, M., Keeley, S., Laloyaux, P., Lopez, P., Lupu, C., Radnoti, G., de Rosnay, P., Rozum, I., Vamborg, F., Villaume, S., and Thépaut, J.-N.: The ERA5 global reanalysis, Q. J. Roy. Meteorol. Soc., 146, 1999–2049, https://doi.org/10.1002/qj.3803, 2020.

Hörhold, M. W., Albert, M. R., and Freitag, J.: The impact of accumulation rate on anisotropy and air permeability of polar firn at a high-accumulation site, J. Glaciol., 55, 625–630, https://doi.org/10.3189/002214309789471021, 2009.

Inoue, R., Fujita, S., Kawamura, K., Oyabu, I., Nakazawa, F., Motoyama, H., and Aoki, T.: Spatial distribution of vertical density and microstructure profiles in near-surface firn around Dome Fuji, Antarctica, The Cryosphere, 18, 425–449, https://doi.org/10.5194/tc-18-425-2024, 2024.

Kinase, T., Adachi, K., Oshima, N., Goto-Azuma, K., Ogawa-Tsukagawa, Y., Kondo, Y., Moteki, N., Ohata, S., Mori, T., Hayashi, M., Hara, K., Kawashima, H., and Kita, K.: Concentrations and Size Distributions of Black Carbon in the Surface Snow of Eastern Antarctica in 2011, J. Geophys. Res. Atmos., 125, e2019JD030737, https://doi.org/10.1029/2019JD030737, 2020.

Leduc-Leballeur, M., Picard, G., Mialon, A., Arnaud, L., Lefebvre, E., Possenti, P., and Kerr, Y.: Modeling L-Band Brightness Temperature at Dome C in Antarctica and Comparison With SMOS Observations, IEEE Trans. Geosci. Remote Sens., 53, 4022–4032, https://doi.org/10.1109/TGRS.2015.2388790, 2015.

Libois, Q., Picard, G., Arnaud, L., Morin, S., and Brun, E.: Modeling the impact of snow drift on the decameter-scale variability of snow properties on the Antarctic Plateau, J. Geophys. Res. Atmos, 119, 11662–11681, https://doi.org/10.1002/2014JD022361, 2014.

Libois, Q., Picard, G., Arnaud, L., Dumont, M., Lafaysse, M., Morin, S., and Lefebvre, E.: Summertime evolution of snow specific surface area close to the surface on the Antarctic Plateau, The Cryosphere, 9, 2383–2398, https://doi.org/10.5194/tc-9-2383-2015, 2015.

Linow, S., Hörhold, M. W., and Freitag, J.: Grain-size evolution of polar firn: a new empirical grain growth parameterization based on X-ray microcomputer tomography measurements, J. Glaciol., 58, 1245–1252, https://doi.org/10.3189/2012JoG11J256, 2012.

Picard, G., Royer, A., Arnaud, L., and Fily, M.: Influence of meter-scale wind-formed features on the variability of the microwave brightness temperature around Dome C in Antarctica, The Cryosphere, 8, 1105–1119, https://doi.org/10.5194/tc-8-1105-2014, 2014.

Picard, G., Libois, Q., Arnaud, L., Verin, G., and Dumont, M.: Development and calibration of an automatic spectral albedometer to estimate near-surface snow SSA time series, The Cryosphere, 10, 1297–1316, https://doi.org/10.5194/tc-10-1297-2016, 2016.

Picard, G., Löwe, H., Domine, F., Arnaud, L., Larue, F., Favier, V., Le Meur, E., Lefebvre, E., Savarino, J., and Royer, A.: The Microwave Snow Grain Size: A New Concept to Predict Satellite Observations Over Snow-Covered Regions, AGU Adv., 3, e2021AV000630, https://doi.org/10.1029/2021AV000630, 2022.

Pirazzini, R., Räisänen, P., Vihma, T., Johansson, M., and Tastula, E.-M.: Measurements and modelling of snow particle size and shortwave infrared albedo over a melting Antarctic ice sheet, The Cryosphere, 9, 2357–2381, https://doi.org/10.5194/tc-9-2357-2015, 2015.

Proksch, M., Löwe, H., and Schneebeli, M.: Density, specific surface area, and correlation length of snow measured by high-resolution penetrometry, J. Geophys. Res. Earth Surf., 120, 346–362, https://doi.org/10.1002/2014JF003266, 2015.

Wiscombe, W. J. and Warren, S. G.: A model for the spectral albedo of snow. I: Pure snow, J. Atmos. Sci., 37, 2712–2733, https://doi.org/10.1175/1520-0469(1980)037<2712:AMFTSA>2.0.CO;2, 1980.